Magnetic carnosine-based metal-organic framework nanoparticles: fabrication, characterization and application as arsenic adsorbent

Maryam Keykhaee[1] · Maryam Razaghi[2] · Arash Dalvand[3] · Fatemeh Salehian[1] · Hamed Soleimani[4] ·
Alireza Samzadeh-Kermani[5] · Hamid Reza Shamsollahi[4] · Alireza Foroumadi[1] · Ali Ramazani[2] · Mehdi Khoobi[1] iD ·
Mahmood Alimohammadi[4]

Abstract

This study centers on the controllable synthesis, characterization, and application of a novel magnetic bio-metal-organic framework (Bio-MOF) for the adsorption and subsequent removal of arsenic from aqueous solutions. Zinc ions and carnosine (Car) were exploited to construct the Car-based MOF on the surface of magnetite (Fe_3O_4 NPs). The Magnetite precoating with Car led to an increase in the yield and the uniform formation of the magnetic MOF. The prepared magnetic Bio-MOF nanoparticles (Fe_3O_4-Car-MOF NPs) had semi-spherical shape with the size in the range of 35–77 nm, and the crystalline pattern of both magnetite and Car-based MOF. The NPs were employed as an adsorbent for arsenic (As) removal. The adsorption analyses revealed that all studied independent variables including pH, adsorbent dose, and initial arsenic concentration had a significant effect on the arsenic adsorption, and the adsorption data were well matched to the quadratic model. The predicted adsorption values were close to the experimental values confirming the validity of the suggested model. Furthermore, adsorbent dose and pH had a positive effect on arsenic removal, whereas arsenic concentration had a negative effect. The adsorption isotherm and kinetic studies both revealed that As adsorption fitted best to the Freundlich isotherm model. The maximum monolayer adsorption capacity (94.33 mg/g) was achieved at room temperature, pH of 8.5 and adsorbent dose of 0.4 g/L. Finally, the results demonstrated that the adsorbent could be efficiently applied for arsenic removal from aqueous environment.

Keywords Peptide-based metal-organic framework · Magnetic nanoparticles · Carnosine · Arsenic removal · Quadratic model

Introduction

With the rapid development of industrialization, inorganic pollutants such as heavy metal ions from wastewater, even at a small scale, have been a serious threat to human health and the ecological systems [43]. One of the most deleterious and toxic heavy metals found in water is Arsenic (As). It is a poisoning element that is introduced as class I carcinogen for human by the international agency for research on cancer (IARC) [13, 18]. Naturally occurring arsenic in rocks and industrial arsenic contained in pesticides are the main sources of water contamination. Because of its carcinogenic character

Authors "Maryam Keykhaee and Maryam Razaghi" have the same contribution to this paper.

✉ Mehdi Khoobi
m-khoobi@tums.ac.ir

✉ Mahmood Alimohammadi
m_alimohammadi@tums.ac.ir

1 Biomaterials Group, Pharmaceutical Sciences Research Center, The Institute of Pharmaceutical Sciences (TIPS), Tehran University of Medical Sciences, Tehran 1417614411, Iran

2 Department of Chemistry, University of Zanjan, Zanjan 4537138791, Iran

3 Environmental Science and Technology Research Center, Department of Environmental Health Engineering, School of Public Health, Shahid Sadoughi University of Medical Sciences, Yazd, Iran

4 Department of Environmental Health Engineering, School of Public Health, Tehran University of Medical Sciences, Tehran, Iran

5 Department of Chemistry, Faculty of Sciences, University of Zabol, Zabol, Iran

and grave health issues for humans, the World Health Organization (WHO) has recommended a standard value for drinking water of 10 μg/L [40].

Not only is arsenic naturally present in the soil and can contaminate surface or underground aquifers, but also anthropological activities such as draining arsenic-containing effluents may increase arsenic concentrations [6, 34]. For this purpose, several removal processes such as chemical precipitation, membrane techniques, ion exchange, adsorption, and electrodialysis (ED) have been applied for As removal from contaminated resources. Among various techniques, adsorption is considered as one of the most efficient processes for drinking water treatment, having advantages such as low cost and ease in operation. Several studies have been conducted to develop numerous natural or synthetic adsorbents for arsenic removal, and some of them are available commercially [7].

As a new class of crystalline inorganic-organic porous hybrid materials, metal-organic frameworks (MOFs) have emerged as a type of promising material for the development of novel adsorbents [20, 24]. These nanomaterials are constructed by multidentate organic ligands and transition metal ions or clusters [44]. Due to the exceptional internal surface area, tailored structure, tunable pore size, and shape of MOFs, the nanomaterials can be easily controlled to facilitate the uptake of a targeted guest molecule [22]. These valuable features of MOF inspired researchers to employ them as catalyst [15], support for gas storage and separation [36], carrier for drug delivery [14, 23], and adsorbent for contaminant removal [25]. However, MOFs suffer from low recyclability and reusability limiting their aplication as an adsorbent in contaminant removal.

Magnetic MOFs overcome the problem and offer practical and versatile process for separating and recycling the adsorbents using exterior magnetic fields [43]. Different strategies have been reported for the preparation of magnetic MOF including Layer-by-Layer (LbL) growth method, embedding method, encapsulation method, and some recently reported method like dry gel conversion strategy, self-template method, magnetic macroporous polymer substrate strategy, seed crystal method, and solvent-free mechanochemical approach [26]. Among different magnetic NPs (MNPs), magnetite (Fe_3O_4) is one of the well-known NPs widely employed in the design and preparation of various adsorbents for chemical pollutants removal [3, 4, 27, 8].

Up to now, a few pioneering studies have been reported related to the removal of heavy metal ions from water by magnetic MOF. Fei Ke et al. reported fabrication of thiol-functionalized porous magnetic MOF as an adsorbent for selective removal of Hg^{2+} and Pb^{2+} from wastewater [30]. In another study, R. Ricco et al. reported aluminum-based magnetic MOF for uptaking Lead (II) from groundwater [21].

Bio-MOFs, which are composed of biomolecules and biocompatible transition metals like zinc or iron, have attracted increasing attention as environmentally benign materials for the application in various branches of science [9, 31]. Peptides are safe and naturally-occurring compounds for the preparation of MOFs endowing the target adsorbent with appropriate biocompatibility, chemical diversity, high flexibility, and excellent adsorption ability for heavy metal removal [16, 28, 32]. L-Carnosine (Car) is a naturally occurring dipeptide located at a high level in nerve tissues and skeletal muscle as a neuropeptide bearing valuable functional groups with the high ability to bind with various metals [5, 11, 19]. These valuable features make Car as a promising multidentate organic bridge for the MOFs preparation and metal removal.

In the light of the facts mentioned above and in continuation of our previous studies on the contaminants removal [1, 37], in this work, a novel magnetic Bio-MOF was introduced for As removal. Fe_3O_4 NPs were employed as a core endowing the target adsorbent with easily separation and recycling. Car-based MOF was exploited as a shell to offer high surface area, appropriate functionality, and porosity to the adsorbent improving As removal. Car coated Fe_3O_4 NPs (Fe_3O_4-Car), and novel magnetic Bio-MOF containing Car and Zinc ions (Fe_3O_4-Car-MOF) were separately prepared and fully characterized. The performance of the designed adsorbents was also evaluated and compared in terms of As removal. To the best of our knowledge, this is the first report on the preparation of magnetic Car-based MOFs and their application for the removal of any contaminants.

Materials and methods

Materials

Iron (III) chloride dihydrate ($FeCl_3.2H_2O$), $FeSO_4.4H_2O$, L-carnosine (Car), zinc nitrate hexahydrate, sodium arsenate, and other materials and reagents were purchased from the Merck Company (Darmstadt, Germany) and used without any further purification.

Synthesis procedure

Car coated Fe_3O_4 MNPs were prepared according to the previously reported method [10]. An aqueous solution of $FeSO_4.4H_2O$ (1.2 g) and $FeCl_3.2H_2O$ (2.34 g) in 100 mL of water was prepared and kept at constant temperature of 80 °C for 30 min under vigorous stirring. 4 g of Car was added to the aqueous solution during 1 h. Then, aqueous ammonia solution was added dropwise to reach pH 11. A black suspension was formed and it was allowed to stir for 1.5 h. All steps were carried out under inert atmosphere and vigorous stirring. Car coated magnetite NPs (Fe_3O_4-Car NPs) were separated from the aqueous solution by magnetic decantation washed with distilled water several times and dried in an oven overnight.

Non-magnetic Car-based MOF was prepared according to the reported method [19].

For the preparation of Fe_3O_4-Car-MOF NPs, aqueous solution of Zn $(NO_3)_2.6H_2O$ (5.26 mL, 0.336 M), aqueous solution of Car (2 mL, 0.442 M), 0.4 g of well-dispersed Fe_3O_4-Car in 2 mL of water and 20 mL of DMF were all combined while stirring. The suspension was heated at 100 °C for 12 h with a ramping rate of 1 °C/min. It was then cooled down to room temperature with a ramping rate of 1 °C/min. The final product was collected by an external magnetic field, washed thoroughly with methanol, and finally dried. The schematic procedure for the preparation of Fe_3O_4-Car-MOF NPs is seen in Fig. 1.

Characterization

The morphology and size of the NPs were determined by field emission scanning electron microscopy (FE-SEM, MIRAIII Tescan). Sample elemental analysis was performed by energy dispersive spectrometry, EDAX (SAMX). The crystal structure of Fe_3O_4-Car-MOF NPs was determined by X-ray powder diffraction, XRD (PHILIPS PW1730 diffractometer using Cu Kα radiation). The FTIR spectra were recorded by a Fourier transform infrared spectrometer, FTIR (Perkin-Elmer) at the wavelength range of 4000–400 cm^{-1} using the KBr pellet technique. Magnetic properties were analyzed using Vibrating Sample Magnetometer, VSM (Meghnatis Daghigh Kavir Co, Iran) with a maximum magnetic field of 10 kOe at 25 °C.

Adsorption test

Sodium arsenate was used for the preparation of arsenic solutions with different concentrations. In each run, a predetermined dose of adsorbent was poured in an Erlenmeyer flask containing a specific concentration of arsenic, and the solution was

agitated on a shaker at a speed of 200 rpm. In all adsorption experiments, the contact time was 180 min, which was the optimum time for the adsorption according to the pretest. At the end of each run, the adsorbent was separated from the solution by an external magnet, and the samples were analyzed by an ICP for the detection of the residual arsenic. All runs were conducted at room temperature.

Isotherm experiments

Langmuir and Freundlich isotherm

The relation between the concentration of adsorbent in the solution and the removed As values were determined by the Langmuir and Freundlich isotherm.

The Langmuir isotherm model is centered on the monolayer distribution of solute molecules onto the surface of the adsorbent. The linear form of the Langmuir model is presented via Eq. (1) [35].

$$\frac{C_e}{q_e} = \frac{1}{K_a q_m} + \frac{C_e}{q_m} \tag{1}$$

q_m, K_a and C_e (the Langmuir constants) representing the maximum adsorption capacity (mg/g), the adsorption energy (L/mg), and equilibrium concentration of As in solution (L/mg) were all calculated from the plot C_e/q_e versus C_e.

The R_L parameter is referred to the non-dimensional constant factor expressing the dependence of the adsorbed substance on the adsorbent and it was calculated using Eq. (2) [35].

$$R_L = \frac{1}{1 + K_a C_0} \tag{2}$$

Where, R_L is dimensionless constant, and C_0 is the initial concentration of As (mg/L).

Fig. 1 Schematic illustration for the preparation of Fe_3O_4-Car-MOF NPs
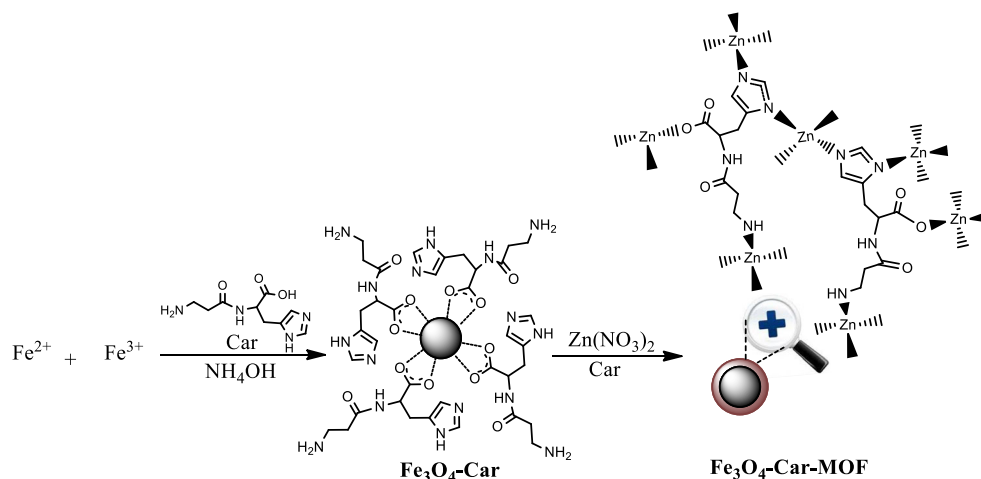
Freundlich isotherm model evaluates the multilayer adsorption of adsorbate on the surface of adsorbent. It also assumes that the adsorption occurs on heterogeneous surfaces expressed via Eq. (3) [29].

$$\log q_e = \log K_f + \frac{1}{n}(\log C_e) \qquad (3)$$

Where, K_f and n are Freundlich constants and q_e is adsorption capacity (mg/g). The adsorption intensity of the system was derived from the plot of $\ln q_e$ versus $\ln C_e$.

Kinetic experiments

Adsorption kinetics of As was assessed by the experimental data [29]. To investigate the mechanism of the adsorption, the transient behavior of the As adsorption process was analyzed using the pseudo-first-order and pseudo-second-order kinetics, explained below:

Pseudo-first-order kinetic The linear form of the pseudo-first-order kinetic model is expressed by Eq. (4) [29].

$$\log(q_e - q_t) = \log(q_e) - \left(\frac{k_1}{2.303}\right)t \qquad (4)$$

Where, q_e, q_t, and k_1 are the amount of adsorbed As at the equilibrium condition (mg/g), the amount of adsorbed As at a given time (t) and the equilibrium rate constant of the pseudo-first-order kinetic model (min^{-1}), respectively. k_1 was obtained from drawing $\log(q_e - q_t)$ versus (t).

Pseudo-second-order kinetic The linear form of pseudo-second-order kinetic was obtained via Eq. (5).

$$\frac{t}{q_t} = \frac{1}{k_2 q_e^2} + \frac{1}{q_e}t \qquad (5)$$

From the plot of (t/q_t) versus (t), the values of the pseudo-second-order rate constants (k_2) (g mg^{-1} min^{-1}) and q_e (mg g^{-1}) was calculated.

The initial adsorption rate (h) was calculated at zero time, via Eq. (6):

$$h = k_2 q_e^2 \qquad (6)$$

Results and discussions

Fe_3O_4-Car and Fe_3O_4-Car-MOF NPs were separately synthesized, and their capacity for the As removal was compared. In our initial attempts to prepare magnetic Car-based MOF, naked Fe_3O_4 MNPs were treated with zinc ions and Car. However, the non-magnetic Bio-MOF was also formed

during the synthesis, decreasing the yield of the target adsorbent. This could be due to the inappropriate affinity of zinc ions to the surface of the Fe_3O_4 MNPs resulting in the nonuniform formation of Bio-MOF. Therefore, in our next attempts, Fe_3O_4 MNPs were initially functionalized with Car to provide an ideal condition for zinc ions immobilization and Bio-MOF formation. To achieve this goal, Fe_3O_4 MNPs were prepared in the presence of Car to endow the surface of the MNPs with appropriate amine and imidazole groups as Zinc chelating agents. Finally, Fe_3O_4-Car NPs were converted to Fe_3O_4-Car-MOF through the hydrothermal formation of MOF by Car and Zinc ions as cationic metal and multidentate organic bridge, respectively (Fig. 1). The prepared NPs were characterized by various methods including FTIR, VSM, XRD, FESEM, EDAX, elemental mapping and TEM analyses. The efficacy of the system was investigated for the As removal from an aqueous environment.

FE-SEM analysis

The morphology and size of the NPs were investigated by FE-SEM and TEM analyses. Figure 2 shows FE-SEM images of the Fe_3O_4-Car and Fe_3O_4-Car-MOF NPs having a semispherical shape and almost monodisperse-size distribution. Fe_3O_4-Car NPs were in the range of 25–45 nm with some agglomeration. The increased size after coating with MOF (about 35–75 nm) could be due to the formation of the layer of Car-based MOF on the surface of Fe_3O_4 MNPs. As can be seen in Fig. 2, the separate particles with almost smooth surfaces confirm that the formation of MOF was accomplished. The TEM images of the NPs revealed agglomerated NPs which could be due to the high tendency of the magnetic NPs to each other due to the dipole-dipole interaction. However, separated spherical NPs with the size of less than 30 nm could be seen in the images. No significant change was observed after formation of MOF on the surface of Fe_3O_4-Car NPs (Fig. 2).

EDAX analysis

Figure 3 depicts FESEM-EDX elemental mapping of Fe_3O_4-Car-MOF NPs. There was no evidence indicating the presence of any impurity within the structure of Fe_3O_4-Car-MOF NPs. The pattern revealed that the NPs were composed of Fe, Zn, C, N, and O elements with the weight ratio of 34.5, 4.5, 17.9, 11.0, and 31.9%, respectively. Appropriate distribution of the elements confirmed successfully preparation of the NPs.

XRD analysis

The crystalline structure and the composition of Fe_3O_4-Car-MOF were also evaluated with single-crystal X-ray diffraction patterns (Fig. 4). The obtained patterns for Fe_3O_4-Car and

Fig. 2 (**a**, **c**) FE-SEM images size distribution histograms determined by Image J 1.44p software (**b**, **d**) and TEM images (**e**, **f**) of Fe_3O_4-Car and Fe_3O_4-Car-MOF NPs, respectively

Fig. 3 FESEM-EDX elemental mapping of Fe_3O_4-Car-MOF NPs
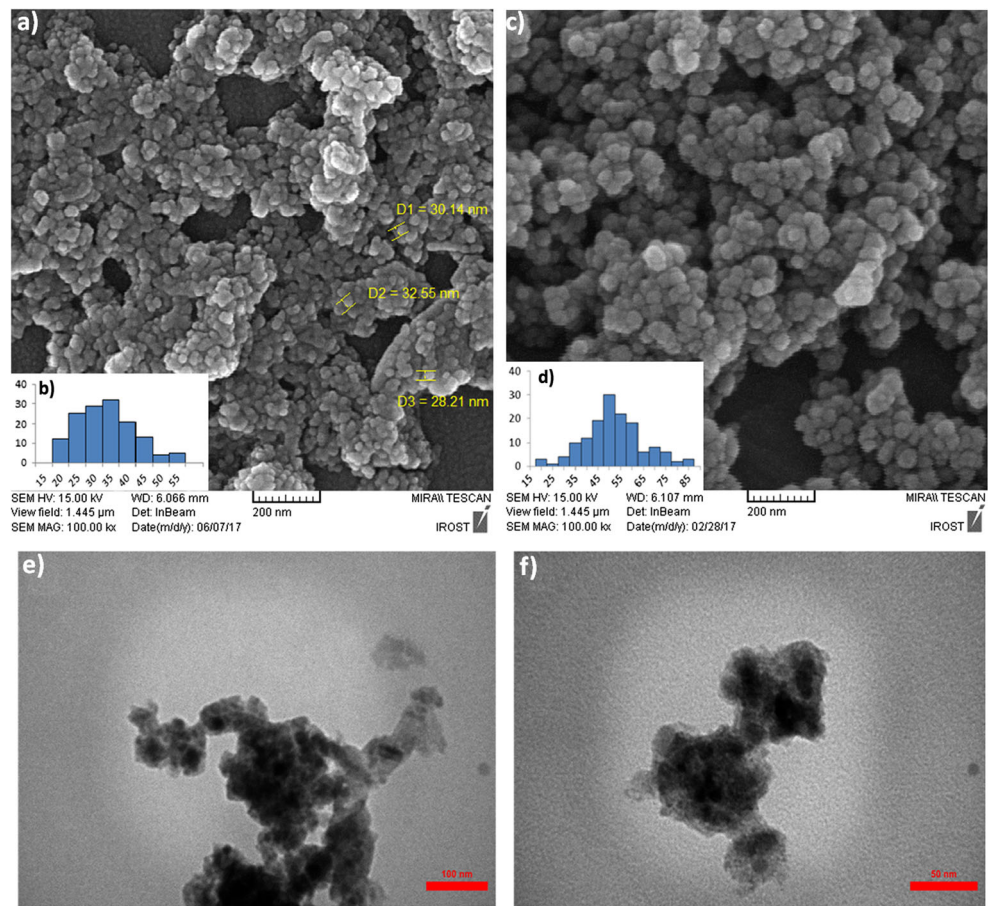
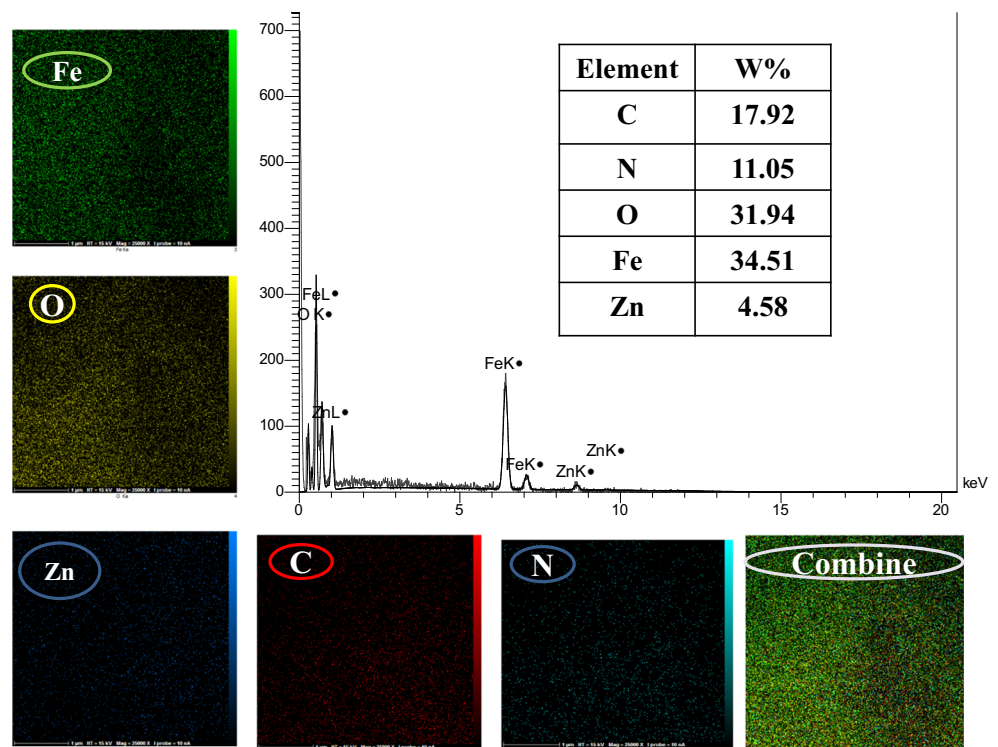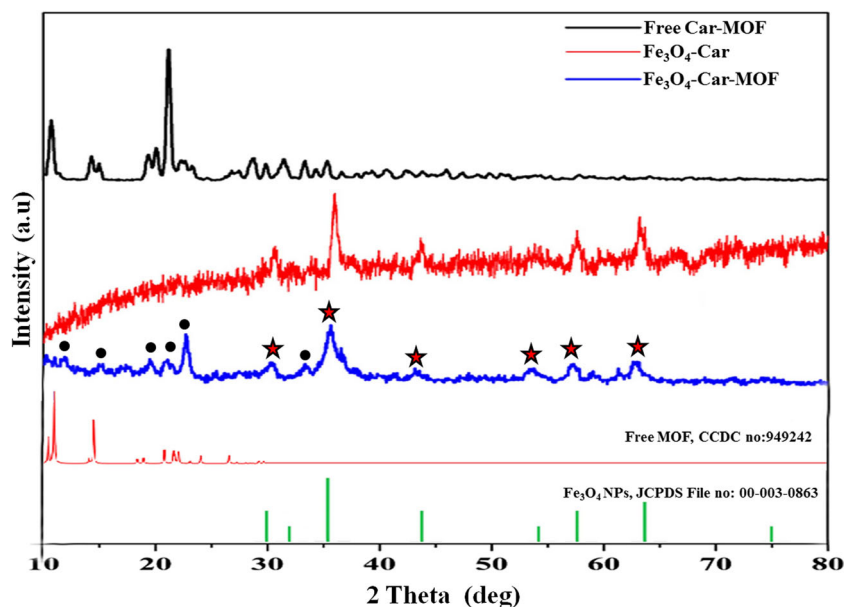| Element	W%
C	17.92
N	11.05
O	31.94
Fe	34.51
Zn	4.58

Fig. 4 XRD patterns of the synthesized NPs and PXRD of the naked Fe_3O_4 and free MOF. Stars and circles show the essential peaks of the naked Fe_3O_4 and free MOF, respectively

Car-based MOF in bulk form (non-magnetic Car-based MOF) were in good agreement with the characterization previously reported elsewhere [19]. The X-ray diffraction pattern of Fe_3O_4-Car-MOF highlights high crystallinity and purity of the product with the specific peaks related to both cubic inverse spinel form of Fe_3O_4 and the MOF. The intensity of the peaks related to the cubic inverse spinel form of Fe_3O_4 NPs was somewhat decreased and broadening was also happened after MOF coating indicating the amorphous structure of the target NPs. The Debye–Scherrer equation was applied for calculating the average crystallite size of Fe_3O_4-Car-MOF:

$$D = \frac{0.9\lambda}{\beta Cos\theta} \tag{7}$$

In this formula, X-ray radiation wavelength (λ) is 0.154059 nm, β represents the corrected band broadening, and θ is referred to the Bragg angle [19]. The average crystalline size of Fe_3O_4-Car-MOF particles was calculated to be about 28 nm using the Debye–Scherrer equation.

The X-ray diffraction patterns of Fe_3O_4-Car demonstrated that the distinct peaks shown at 2θ of 30°, 36°, 43°, 54°, 57°, 63° are attributed to the (220), (311), (400) (422), (511), (440) planes of Fe_3O_4 which was also observed in the pattern of Fe_3O_4-Car-MOF. The essential crystalline plates of the Car-based MOF were also identified with a slight shift in the diffraction pattern of Fe_3O_4-Car-MOF reaffirming the successful formation of the MOF on the surface of Fe_3O_4 MNPs.

FTIR analysis

The FTIR spectroscopy was applied to determine the type of functional groups in the structure of Fe_3O_4-Car-MOF. Figure 5

shows the FT-IR spectra of Fe_3O_4-Car and Fe_3O_4-Car-MOF NPs. In the FTIR spectra of Fe_3O_4-Car and Fe_3O_4-Car-MOF, the peak appeared at about 580 cm^{-1} is related to the stretching vibration of the Fe-O bond of Fe_3O_4 MNPs. The broad peak appeared at 3386 cm^{-1} could be related to the hydroxyl groups of the MNPs which was probably overlapped by the stretching vibration of NH$_2$ group of Car. The bands attributed to the stretching vibrations of carboxylate bonds (COO$^-$), which presumably interacted with the surface of Fe_3O_4 and C=O amide bonds, are shown at 1630 and 1617 cm^{-1}, respectively. The stretching frequencies of asymmetric and symmetric CH$_2$ groups of Car were also observed at 2848 and 2922 cm^{-1} [10]. In the FTIR spectrum of Fe_3O_4-Car-MOF NPs, an apparent increase in the amplitude of the NH amide bond at 1622 cm^{-1} and C=N
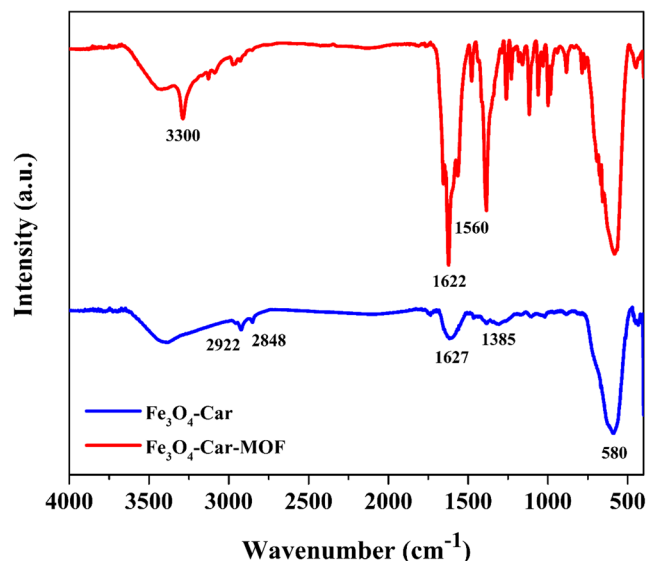

Fig. 5 FTIR spectra of Fe_3O_4-Car and Fe_3O_4-Car-MOF NPs

bond of imidazole ring at 1560 cm^{-1} could confirm the large presence of Car as well as the successful formation of the MOF. Also, the peak at 3300 cm^{-1} could be probably due to the stretching frequencies of the N-H bond of Car. These results along with the results of EDAX and XRD analyses confirm the successful formation of the magnetic-based MOF.

VSM analysis

The magnetic property of Fe$_3$O$_4$-Car-MOF NPs was measured using VSM at room temperature and compared with the naked Fe$_3$O$_4$ and Fe$_3$O$_4$-Car NPs (Fig. 6). The applied magnetic field was varied from −9 kOe to 9 kOe. The magnetization curve did not exhibit hysteresis and coercivity. This observation indicated that NPs had superparamagnetic behavior. The saturation magnetization values for Fe$_3$O$_4$-Car and Fe$_3$O$_4$-Car-MOF were found to be 33 and 28 emu/g at room temperature, respectively. The meaningful drop in the magnetization value of Fe$_3$O$_4$-Car-MOF could be attributed to the non-magnetic character of Zinc and Car.

As removal

Experimental design

Initial attempts to evaluate the efficacy of the NPs revealed that Fe$_3$O$_4$-Car-MOF had higher potential for As removal than Fe$_3$O$_4$-Car (about 17% more than Fe$_3$O$_4$-Car). Therefore, magnetic bio-MOF was employed for the next studies. The effect of independent variables such as adsorbent dose (0.1–0.4 g/l), pH (3–11), and initial arsenic concentration (20–40 mg/L) on the arsenic adsorption was investigated in a batch system. Central composite design (CCD) under response surface methodology was applied for the determination of the number of runs, studying the interaction of parameters, and analyzing the experimental data [2, 17].

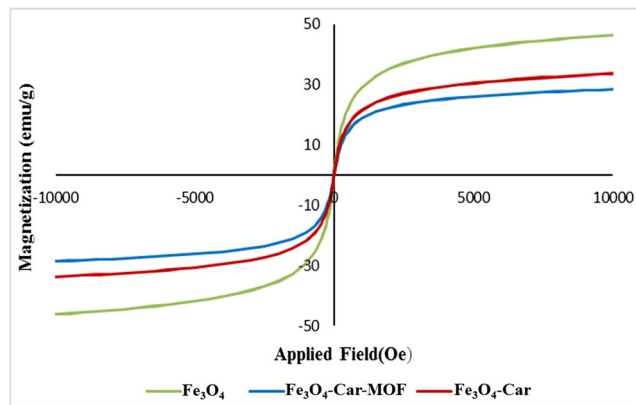According to the central composite design, 29 experiments were selected for investigating the effect of three different variables on the arsenic adsorption. To analyze the results, Design-Expert software (version 7, trial, Stat-Ease) was utilized [35]. Table 1 shows the central composite design matrix for the arsenic adsorption and the adsorption data. As seen in Table 1, the predicted adsorption values are close to the experimental values confirming the validity of the quadratic model.

Analysis of variance results

According to the data presented in Table 2, all studied independent variables have a significant effect (p value <0.05) on the arsenic removal, and the quadratic model is significant (R squared 0.8868, p value <0.0001, and lack of fit 0.0509) [39]. Based on the F value, the adsorbent dose is the most important parameter in the arsenic adsorption.

Based on the acquired regression coefficients, the arsenic removal efficiency can be computed by Eq. (8)

Table 1 Central composite design matrix for arsenic adsorption

Run order	A (Adsorbent dose)	B (pH)	C (As concentration)	As removal (%)	
				Experimental	Predicted
1	0	0	0	63	59.2
2	0	0	0	62	59.2
3	−0.5	0.5	0.5	35	37.3
4	0	0	0	53	59.2
5	−0.5	−0.5	0.5	22	17.7
6	−0.5	0.5	−0.5	48	56.2
7	0.5	0.5	−0.5	72	81.6
8	0.5	−0.5	0.5	56	53.1
9	0	0	0	67	59.2
10	0.5	−0.5	−0.5	71	73.9
11	0	0	0	60	59.2
12	−0.5	−0.5	−0.5	32	37.1
13	0	0	0	54	59.2
14	0.5	0.5	0.5	61	61.2
15	0	0	0	67	59.2
16	0	0	1	23	27.9
17	0	0	0	68	59.2
18	1	0	0	89	86.7
19	0	0	0	58	59.2
20	0	0	0	52	59.2
21	0	0	0	59	59.2
22	0	0	0	60	59.2
23	0	0	−1	78	67.7
24	0	−1	0	30	32.2
25	0	1	0	67	59.4
26	0	0	0	58	59.2
27	0	0	0	62	59.2
28	0	0	0	51	59.2
29	−1	0	0	29	25.9

Fig. 6 Magnetization curves of Fe$_3$O$_4$, Fe$_3$O$_4$-Car and Fe$_3$O$_4$-Car-MOF NPs at room temperature

Table 2 ANOVA results for arsenic removal using Fe$_3$O$_4$-Car-MOF

Source	Sum of squares	df	Mean square	F value	p value
Model	6678.84	9	742.09	16.55	<0.0001
A-Adsorbent dose	3690.56	1	3690.56	82.28	<0.0001
B-pH	742.56	1	742.56	16.56	0.0007
C-As concentration	1580.06	1	1580.06	35.23	<0.0001
AB	66.13	1	66.13	1.47	0.2395
AC	1.13	1	1.13	0.025	0.8758
BC	0.13	1	0.13	2.787E-003	0.9584
A^2	16.59	1	16.59	0.37	0.5502
B^2	350.40	1	350.40	7.81	0.0115
C^2	253.74	1	253.74	5.66	0.0280
Residual	852.20	19	44.85		
Lack of fit	436.60	5	87.32	2.94	0.0509
Pure error	415.60	14	29.69		
Cor total	7531.03	28			

R-Squared: 0.886, Adj R-Squared: 0.833

As removal $(\%) = +59.24 + 18.06*A$
$+ 8.10*B - 11.82*C - 4.07*A*B - 0.53*A*C$
$+ 0.18*B*C - 1.03*A^2 - 4.74*B^2 - 4.04*C^2$
$$(8)$$

Where; A, B, and C are the coded levels of adsorbent dose, pH, and arsenic concentration, respectively. The regression data showed that adsorbent dose and pH had a positive effect on the arsenic adsorption, whereas initial arsenic concentration had a negative effect.
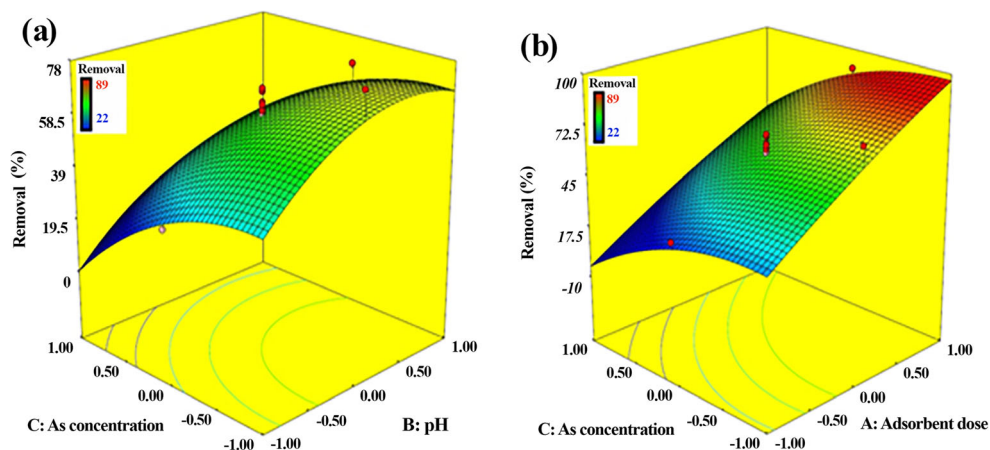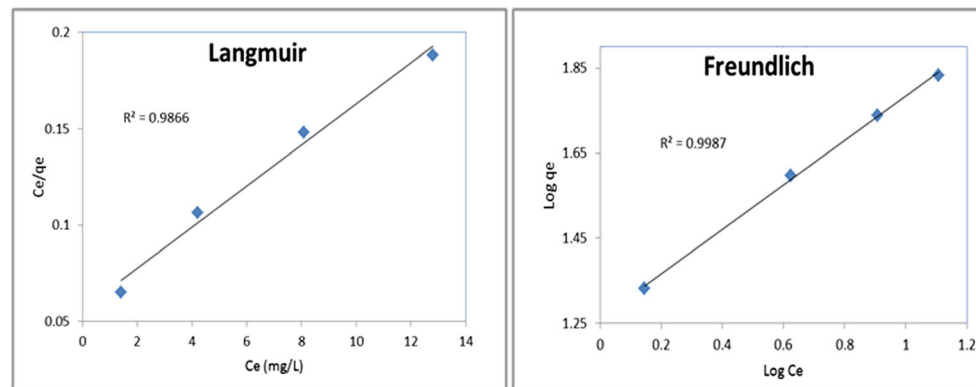

Fig. 7 Three-dimensional plots: Arsenic removal efficiency as the function of independent parameters; (a) As concentration/pH; (b) As concentration/ adsorbent dose

Fig. 8 The plots for the Langmuir and Freundlich isotherm models regarding the adsorption of As on Fe$_3$O$_4$-Car-MOF NPs

Table 3 Freundlich and Langmuir isotherm parameters for adsorption of As

Parameters	Langmuir	Freundlich
K_L (L/mg)	0.18	18.24
Q_m	94.33	–
R_L	0.34	–
R^2	0.9866	0.9987
n	–	1.91

Table 4 Pseudo-first-order and pseudo-second-order kinetic parameters regarding adsorption of As

Parameters	Q_e mg g^{-1} (Cal.)	Q_e mg g^{-1} (Exp.)	k_1 (min^{-1})	k_2 (g mg^{-1} min^{-1})	R^2
Pseudo-first-order kinetic	12.28	39.5	0.011		0.208
Pseudo-second-order kinetic	38.91	39.5		0.002	0.942

Effect of independent variables

The effect of independent variables on the arsenic removal is seen in Fig. 7. It is clear that higher As removal could be achieved through the rise in the adsorbent dose and pH values as well as the drop in the As concentration. In other words, when the adsorbent dose increases the number of available active sites for the adsorption of arsenic ions increases, which results in the improvement of arsenic adsorption [42]. However, with increasing the concentration of arsenic the number of active sites is not enough to remove all arsenic ions, and eventually, the adsorption efficiency declines. In a related study, a similar trend was reported for the effect of pH on the arsenic removal using octanuclear Zn (II)-based polymer [41]. The maximum monolayer adsorption capacity was 94.33 mg/g and the optimum condition was obtained at room temperature, pH of 8.5 and adsorbent dose of 0.4 g/L.

## Langmuir and Freundlich isotherm models

Figure 8 and Table 4 show the Langmuir isotherm and the concerning kinetic parameters of Fe_3O_4-Car-MOF NPs. A good coefficient of determination was achieved for the Langmuir isotherm ($R^2 = 0.9866$). q_m, K_a and R_L (the Langmuir constants) were determined to be 94.33, 2 and 0.013 mg/g, respectively. The R_L is referred to the relative volatility in vapour–liquid equilibrium. The amount of R_L determines the type of equilibrium as follows: $0 < R_L < 1$ refers to the favorable equilibrium, whilst $R_L > 1$ is attributed to the unfavorable isotherm [12].

The adsorption data were also analyzed using the Freundlich isotherm, and the results are presented in Table 3. K_f and n, known as the Freundlich constants, were calculated from the plot of lnq_e versus lnC_e, which were 12.3 mg g^{-1} and 1.91, respectively. Also, the coefficient of determination (R^2) for the Freundlich isotherm was 0.9987 (Table 3). The value of n was larger than one indicating a favorable adsorption system. With comparison of coefficient of determinations (R^2) of the two models involved, it could be deducted that Freundlich model fitted best to describe the adsorption process in this study. In a similar related study, the same behavior was also observed for the methylene blue adsorption onto activated carbon prepared from rattan sawdust and jute fiber carbon [12, 33].

Kinetics of adsorption

In this study, the applicability of the pseudo-first-order and pseudo-second-order models was tested for the adsorption of As, and the results showed that the pseudo-second-order model provided a very good coefficient of determination (R^2) (Fig. 9 and Table 4). The value of the calculated equilibrium adsorption capacity (q_e) from the pseudo-first-order model was significantly lower than the experimental q_e value indicating the inapplicability of the model. For the pseudo-second-order kinetic model, the high coefficient of determination (R^2), and the closeness of the calculated q_e from the model to the experimental q_e value indicate that the model is highly applicable to describe the adsorption of As on the adsorbent [38]. These results are in line with the previously reported

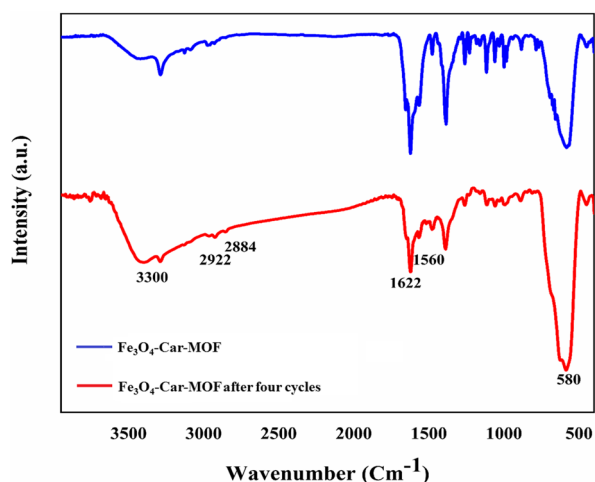**Fig. 9** (a) Pseudo-first-order, and (b) pseudo-second-order kinetic plots for the adsorption of As
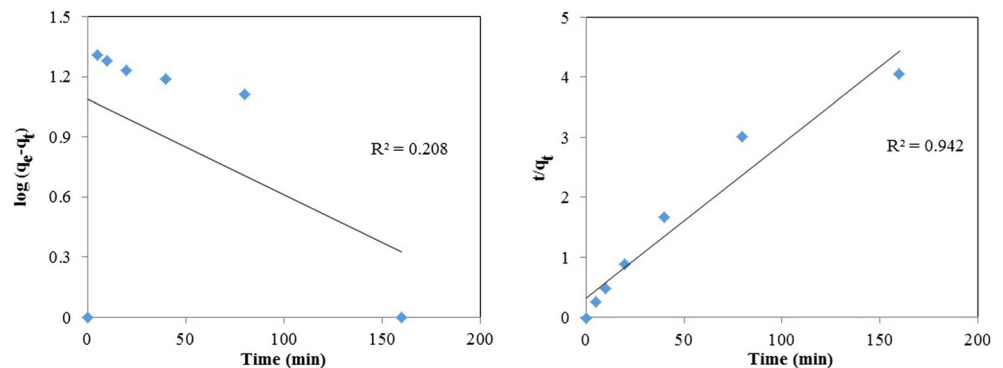
Fig. 10 FTIR spectra of Fe$_3$O$_4$-Car-MOF NPs and Fe$_3$O$_4$-Car-MOF NPs after 4 cycles

studies such as adsorption of As onto rice husk [38] and bamboo-based activated carbon [12].

Stability of the adsorbent

Stability of the Fe$_3$O$_4$-Car-MOF was evaluated in simulated media for As removal. A predetermined dose of adsorbent (0.4 g/L) was poured in an Erlenmeyer flask containing a specific concentration of As, and the solution was agitated on a shaker at a speed of 200 rpm for 180 min, pH 8.5 at room temperature, which were the optimum parameters for the adsorption according to the pretest. At the end of each run, the adsorbent was separated from the solution by an external magnet. Four cycles of regeneration studies were carried out. FTIR analysis of the fresh Fe$_3$O$_4$-Car-MOF and the adsorbent after 4 cycles were compared with each other. The results clearly suggested stability of the adsorbent without any significant changes in the essential functional groups of the NPs (Fig. 10).

Conclusions

In this study, a simple, rapid, and cost-effective method with no need to template, surfactant and catalyst was introduced for the synthesis of a novel magnetic Bio-MOF (Fe$_3$O$_4$-Car-MOF NPs) employed for the arsenic adsorption from aqueous solution. Fully characterization of the NPs confirmed formation of nearly spherical NPs with the size in the range of 35–77 nm bearing both character of the cubic inverse spinel form of Fe$_3$O$_4$ and Car-based MOF and appropriate elemental distribution. According to the statistical results, all studied independent parameters had a significant effect on the arsenic adsorption (p value <0.05), and the regression data indicated that adsorbent dose and pH had a positive effect on the arsenic adsorption, whereas initial arsenic concentration had a

negative effect. Based on the fisher value, the adsorbent dose was the most influential parameter in the arsenic adsorption. The experimental data were well fitted to the quadratic model, and Fe$_3$O$_4$-Car-MOF NPs were able to remove arsenic up to 89%. The optimum condition was obtained at room temperature, pH of 8.5 and adsorbent dose of 0.4 g/L resulted in the maximum monolayer adsorption capacity of 94.33 mg/g. The preliminary screening exhibited appropriate stability of the NPs after four cycles without any significant changes in the functional grooups of the NPs. However, more studies are suggested to evaluate reusability and stability of the adsorbent. Finally, it is assumed that the magnetic Bio-MOF could be successfully employed for the removal of other contaminants and its application might be potentially extended to further areas of interest such as drug delivery and medical imaging.

Compliance with ethical standards

Conflict of interest　　The authors declare no conflict of interest.

References

1. Ansari A, Vahedi S, Tavakoli O, Khoobi M, Faramarzi MA. Novel Fe3O4/hydroxyapatite/β-cyclodextrin nanocomposite adsorbent: synthesis and application in heavy metal removal from aqueous solution. Appl Organomet Chem. 2019;33 https://doi.org/10.1002/aoc.4634.

2. Ashrafi S, Nasseri S, Alimohammadi M, Mahvi A, Faramarzi M. Optimization of the enzymatic elimination of flumequine by laccase-mediated system using response surface methodology. Desalin Water Treat. 2016;57:14478–87. https://doi.org/10.1080/19443994.2015.1063462.

3. Badi MY, Azari A, Pasalari H, Esrafili A, Farzadkia M. Modification of activated carbon with magnetic Fe3O4 nanoparticle composite for removal of ceftriaxone from aquatic solutions. J Mol Liq. 2018;261:146–54. https://doi.org/10.1016/j.molliq.2018.04.019.

4. Baziar M, Azari A, Karimaei M, Gupta VK, Agarwal S, Sharafi K, Maroosi M, Shariatifar N, Dobaradaran S. MWCNT-Fe3O4 as a superior adsorbent for microcystins LR removal: investigation on the magnetic adsorption separation, artificial neural network modeling, and genetic algorithm optimization. J Mol Liq. 2017;241:102–13. https://doi.org/10.1016/j.molliq.2017.06.014.

5. Brown WE, Schroeder LW, Ferris JS. Interlayering of crystalline octacalcium phosphate and hydroxylapatite. JPhCh. 1979;83:3314–9. https://doi.org/10.1021/j100489a002.

6. Cheng Z, Fu F, Dionysiou DD, Tang B. Adsorption, oxidation, and reduction behavior of arsenic in the removal of aqueous As (III) by mesoporous Fe/Al bimetallic particles. Water Res. 2016;96:22–31. https://doi.org/10.1016/j.watres.2016.03.020.

7. Chirenje T, Ma LQ, Chen M, Zillioux EJ. Comparison between background concentrations of arsenic in urban and non-urban areas of Florida. Adv Environ Res. 2003;8:137–46. https://doi.org/10.1016/S1093-0191(02)00138-7.

8. Dobaradaran S. Nabizadeh Nodehi R. Yaghmaeian K. Jaafari J. Hazrati Niari M. Kumar Bharti A. Agarwal Sh. Kumar Gupta V. Azari A. Shariatifar N. Catalytic decomposition of 2-chlorophenol using an ultrasonic-assisted Fe 3 O 4–TiO 2@ MWCNT system: influence factors, pathway and mechanism study. J Colloid Interface Sci. 2018;512:172–189. https://doi.org/10.1016/j.jcis.2017.10.015.

9. Doonan C, Riccò R, Liang K, Bradshaw D, Falcaro P. Metal–organic frameworks at the biointerface: synthetic strategies and applications. Acc Chem Res. 2017;50:1423–32. https://doi.org/10.1021/acs.accounts.7b00090.

10. Durmus Z, Kavas H, Baykal A, Sozeri H, Alpsoy L, Çelik S, Toprak M. Synthesis and characterization of l-carnosine coated iron oxide nanoparticles. JAllC. 2011;509:2555–61. https://doi.org/10.1016/j.jallcom.2010.11.088.

11. Gholibegloo E, Karbasi A, Pourhajibagher M, Chiniforush N, Ramazani A, Akbari T, Bahador A, Khoobi M. Carnosine-graphene oxide conjugates decorated with hydroxyapatite as promising nanocarrier for ICG loading with enhanced antibacterial effects in photodynamic therapy against Streptococcus mutans. J Photochem Photobiol B Biol. 2018;181:14–22. https://doi.org/10.1016/j.jphotobiol.2018.02.004.

12. Hameed B, Din AM, Ahmad A. Adsorption of methylene blue onto bamboo-based activated carbon: kinetics and equilibrium studies. J Hazard Mater. 2007;141:819–25. https://doi.org/10.1016/j.jhazmat.2006.07.049.

13. Holkar CR, Jadhav AJ, Pinjari DV, Mahamuni NM, Pandit AB. A critical review on textile wastewater treatments: possible approaches. J Environ Manag. 2016;182:351–66. https://doi.org/10.1016/j.jenvman.2016.07.090.

14. Horcajada P, Chalati T, Serre C, Gillet B, Sebrie C, Baati T, Eubank JF, Heurtaux D, Clayette P, Kreuz C. Porous metal–organic-framework nanoscale carriers as a potential platform for drug delivery and imaging. Nat Mater. 2010;9:172–8. https://doi.org/10.1038/nmat2608.

15. Hu P, Morabito JV, Tsung C-K. Core–shell catalysts of metal nanoparticle core and metal–organic framework shell. ACS Catal. 2014;4:4409–19. https://doi.org/10.1021/cs5012662.

16. Imaz I, Rubio-Martínez M, An J, Sole-Font I, Rosi NL, Maspoch D. Metal–biomolecule frameworks (MBioFs). ChCom. 2011;47:7287–302. https://doi.org/10.1039/C1CC11202C.

17. Javid A, Nasseri S, Mesdaghinia A, Hossein Mahvi A, Alimohammadi M, Aghdam RM, Rastkari N. Performance of photocatalytic oxidation of tetracycline in aqueous solution by TiO 2 nanofibers. J Environ Health Sci Eng. 2013;11:24.

18. Jomova K, Jenisova Z, Feszterova M, Baros S, Liska J, Hudecova D, Rhodes C, Valko M. Arsenic: toxicity, oxidative stress and human disease. J Appl Toxicol. 2011; https://doi.org/10.1002/jat.1649.

19. Katsoulidis AP, Park KS, Antypov D, Martí-Gastaldo C, Miller GJ, Warren JE, Robertson CM, Blanc F, Darling GR, Berry NG. Guest-adaptable and water-stable peptide-based porous materials by Imidazolate side chain control. Angew Chem. 2014;53:193–8. https://doi.org/10.1002/anie.201307074.

20. Ke F, Luo G, Chen P, Jiang J, Yuan Q, Cai H, Peng C, Wan X. Porous metal–organic frameworks adsorbents as a potential platform for defluoridation of water. JPMat. 2016;23:1065–73. https://doi.org/10.1007/s10934-016-0164-5.

21. Ke F, Jiang J, Li Y, Liang J, Wan X, Ko S. Highly selective removal of Hg2+ and Pb2+ by thiol-functionalized Fe3O4@ metal-organic framework core-shell magnetic microspheres. ApSS. 2017;413:266–74. https://doi.org/10.1016/j.apsusc.2017.03.303.

22. Ke F, Peng C, Zhang T, Zhang M, Zhou C, Cai H, Zhu J, Wan X. Fumarate-based metal-organic frameworks as a new platform for highly selective removal of fluoride from brick tea. Sci Rep. 2018;8:939. https://doi.org/10.1038/s41598-018-19277-2.

23. Ke F, Zhang M, Qin N, Zhao G, Chu J, Wan X. Synergistic anti-oxidant activity and anticancer effect of green tea catechin stabilized on nanoscale cyclodextrin-based metal–organic frameworks. JMatS. 2019;54:10420–9. https://doi.org/10.1007/s10853-019-03604-7.

24. Khan NA, Jhung SH. Adsorptive removal and separation of chemicals with metal-organic frameworks: contribution of π-complexation. J Hazard Mater. 2017;325:198–213. https://doi.org/10.1016/j.jhazmat.2016.11.070.

25. Khan NA, Hasan Z, Jhung SH. Adsorptive removal of hazardous materials using metal-organic frameworks (MOFs): a review. J Hazard Mater. 2013;244–245:444–56. https://doi.org/10.1016/j.jhazmat.2012.11.011.

26. Ma YJ, Jiang XX, Lv YK. Recent advances in preparation and applications of magnetic framework composites. Chem–Asian J. 2019; https://doi.org/10.1002/asia.201901139.

27. Mesdaghinia A, Azari A, Nodehi RN, Yaghmaeian K, Bharti AK, Agarwal S, Gupta VK, Sharafi K. Removal of phthalate esters (PAEs) by zeolite/Fe3O4: investigation on the magnetic adsorption separation, catalytic degradation and toxicity bioassay. J Mol Liq. 2017;233:378–90. https://doi.org/10.1016/j.molliq.2017.02.094.

28. Nejadshafiee V, Naeimi H, Goliaei B, Bigdeli B, Sadighi A, Dehghani S, Lotfabadi A, Hosseini M, Nezamtaheri MS, Amanlou M. Magnetic bio-metal–organic framework nanocomposites decorated with folic acid conjugated chitosan as a promising biocompatible targeted theranostic system for cancer treatment. Mater Sci Eng C. 2019;99:805–15. https://doi.org/10.1016/j.msec.2019.02.017.

29. Pourkarim S, Ostovar F, Mahdavianpour M, Moslemzadeh M. Adsorption of chromium (VI) from aqueous solution by artist's bracket fungi. SS&T. 2017;52:1733–41. https://doi.org/10.1080/01496395.2017.1299179.

30. Prathna T, Sharma SK, Kennedy M. Nanoparticles in household level water treatment: an overview. Sep Purif Technol. 2018;199:260–70. https://doi.org/10.1016/j.seppur.2018.01.061.

31. Ricco R, Konstas K, Styles MJ, Richardson JJ, Babarao R, Suzuki K, Scopece P, Falcaro P. Lead (II) uptake by aluminium based magnetic framework composites (MFCs) in water. J Mater Chem A. 2015;3:19822–31. https://doi.org/10.1039/C5TA04154F.

32. Rojas S, Devic T, Horcajada P. Metal organic frameworks based on bioactive components. J Mater Chem B. 2017;5:2560–73. https://doi.org/10.1039/C6TB03217F.

33. Senthilkumaar S, Varadarajan P, Porkodi K, Subbhuraam CV. Adsorption of methylene blue onto jute fiber carbon: kinetics and equilibrium studies. J Colloid Interface Sci. 2005;284:78–82. https://doi.org/10.1016/j.jcis.2004.09.027.

34. Sigdel A, Park J, Kwak H, Park P-K. Arsenic removal from aqueous solutions by adsorption onto hydrous iron oxide-impregnated alginate beads. J Ind Eng Chem. 2016;35:277–86. https://doi.org/10.1016/j.jiec.2016.01.005.

35. Soleimani H, Mahvi AH, Yaghmaeian K, Abbasnia A, Sharafi K, Alimohammadi M, Zamanzadeh M. Effect of modification by five different acids on pumice stone as natural and low-cost adsorbent for removal of humic acid from aqueous solutions-application of response surface methodology. J Mol Liq. 2019;290:111181. https://doi.org/10.1016/j.molliq.2019.111181.

36. Spanopoulos I, Tsangarakis C, Klontzas E, Tylianakis E, Froudakis G, Adil K, Belmabkhout Y, Eddaoudi M, Trikalitis PN. Reticular synthesis of HKUST-like tbo-MOFs with enhanced CH4 storage. J Am Chem Soc. 2016;138:1568–74. https://doi.org/10.1021/jacs.5b11079.

37. Tapouk FA, Nabizadeh R, Nasseri S, Mesdaghinia A, Khorsandi H, Mahvi AH, Gholibegloo E, Alimohammadi M, Khoobi M. Endotoxin removal from aqueous solutions with dimethylamine-functionalized graphene oxide: modeling study and optimization

of adsorption parameters. J Hazard Mater. 2019;368:163–77. https://doi.org/10.1016/j.jhazmat.2019.01.028.

38. Vadivelan V, Kumar KV. Equilibrium, kinetics, mechanism, and process design for the sorption of methylene blue onto rice husk. JCIS. 2005;286:90–100. https://doi.org/10.1016/j.jcis.2005.01.007.

39. Verbruggen S, De Sutter S, Iliopoulos S, Aggelis D, Tysmans T. Experimental structural analysis of hybrid composite-concrete beams by digital image correlation (DIC) and acoustic emission (AE). JNE. 2016; https://doi.org/10.1007/s1092.

40. Wan W, Pepping TJ, Banerji T, Chaudhari S, Giammar DE. Effects of water chemistry on arsenic removal from drinking water by electrocoagulation. Water Res. 2011;45:384–92. https://doi.org/10.1016/j.watres.2010.08.016.

41. Xiao Y, Zhang C, Qin Y, Wu C, Zheng X. Highly efficient removal of As (V) from aqueous solutions using a novel octanuclear Zn (II)-based polymer: synthesis, structure, properties and optimization

using a response surface methodology. J Solid State Chem. 2018;264:6–14. https://doi.org/10.1016/j.jssc.2018.04.030.

42. Zarei H, Nasseri S, Nabizadeh R, Shemirani F, Dalvand A, Mahvi AH. Modeling of arsenic removal from aqueous solution by means of MWCNT/alumina nanocomposite. Desalin Water Treat. 2017;67:196–205. https://doi.org/10.5004/dwt.2017.20402.

43. Zhao G, Qin N, Pan A, Wu X, Peng C, Ke F, Iqbal M, Ramachandraiah K, Zhu J. Magnetic nanoparticles@ metal-organic framework composites as sustainable environment adsor-bents. J Nanomater. 2019;2019:1–11. https://doi.org/10.1155/2019/1454358.

44. Zhu Q-L, Xu Q. Metal–organic framework composites. ChSRv. 2014;43:5468–512. https://doi.org/10.1039/C3CS60472A.